Bond Model Development for Pretensioned Concrete Crossties with User Materials in Abaqus

Hailing Yu, and David Y. Jeong

Volpe National Transportation Systems Center

Abstract: *Pretensioned concrete crossties are increasingly employed in railroad heavy haul and high speed lines. The bond between steel reinforcements and concrete affects several important performance measures of concrete ties, and bond modeling is a critical component in the analysis of concrete tie behavior using the finite element (FE) method. This paper summarizes the bond models developed at the Volpe Center for pretensioned concrete crossties and their implementation as user materials for cohesive elements in Abaqus. The bond models are macro-scale or phenomenological and developed within the elasto-plastic framework. The steel reinforcement-concrete interface is homogenized and represented with a thin layer of cohesive elements sandwiched between steel and concrete elements. Traction-displacement constitutive or bond relations are defined and assigned for the cohesive elements. The traction components are normal and shear stresses, and the displacement components are interfacial dilatation and slip. Elasto-plastic bond models for a smooth wire, three indented wires and a seven-wire strand commonly used in concrete crosstie production are presented with their respective elastic stiffness, yield function and plastic flow definitions. Calibration and validation of these bond models with experimental data are further described in this paper.*

Keywords: *Pretensioned Concrete Crosstie, Smooth Wire, Indented Wire, Seven-Wire Strand, Elasto-Plastic Bond Model, User Material, Cohesive Element, Calibration, Validation.*

1. Introduction

Concrete crossties are pretensioned members made by embedding prestressing steel reinforcements in concrete and releasing the pretension in the reinforcements when desired concrete strength is reached. They are increasingly employed in railroad heavy haul and high speed lines to achieve improved durability performance and longer service lives. The interaction between steel reinforcements and concrete, commonly referred to as bond, can affect several important concrete tie performance measures, including transfer length, bursting or splitting propensity and flexural moment capacity. Kansas State University (KSU) studied the bond and transfer length characteristics of 15 selected prestressing wires and strands for concrete ties using the experimental methods (Arnold, 2013; Bodapati, 2013a,b; Zhao, 2014). Figure 1 shows the microscopic images and 3D models (Haynes, 2013) of a smooth wire (WA), three indented wires (WE, WG and WH) and a seven-wire strand (SA) studied by KSU researchers. The Volpe Center has been developing macro-scale or phenomenological bond models for the finite element analyses (FEA) of concrete crossties (Yu and Jeong, 2014, 2015 and 2016). This paper summarizes the bond models developed at the Volpe Center and model calibration and validation based on KSU experimental data for the wires and strand shown in Figure 1.

The primary bond mechanisms of prestressing wires or strands are adhesion, mechanical interaction and friction. The bond stress evolves with the relative slip in the steel-concrete interface. In addition, there can be dilatational effects resulting from pretension release and interfacial slips. When the pretension is released during the manufacturing process, the wires or strands dilate radially due to Hoyer effect as the stress reduces in the reinforcements. With the exception of the smooth wire, the reinforcements shown in Figure 1 have uneven surfaces: the wires with spiral or chevron indents and the strand with natural spiral surfaces. The concrete surface originally matches the surface shapes of the reinforcements. When the reinforcement and concrete slip relative to each other, the surfaces become mismatched and produce additional normal dilation (or dilatation) along the steel-concrete interface. In the macro-scale or phenomenological bond modeling approach adopted in this study, the non-smooth surfaces are homogenized and represented with a thin interface layer sandwiched between the steel reinforcements and the concrete. A phenomenological bond model is expected to reproduce the bond-slip and dilatational effects even with the homogenized interfaces. A thin interface layer is applied for the smooth surfaces as well to account for the effects of adhesion and friction.

This paper first describes the elasto-plastic framework for bond modeling, including governing equations, solution approach and bond model definitions (yield function, plastic flow rule and identification of bond material constants). Second, the model calibration process is described, and calibrated bond material constants are presented based on untensioned pullout and pretensioned prism tests conducted on concrete specimens at KSU. Third, simulation results from the calibrated bond models are validated with surface strain data measured on actual concrete crossties made at a tie manufacturing plant. Last, a summary of the work and main conclusions are presented. A schematic of the FEA bond modeling framework employed in this paper is shown in Figure 2.

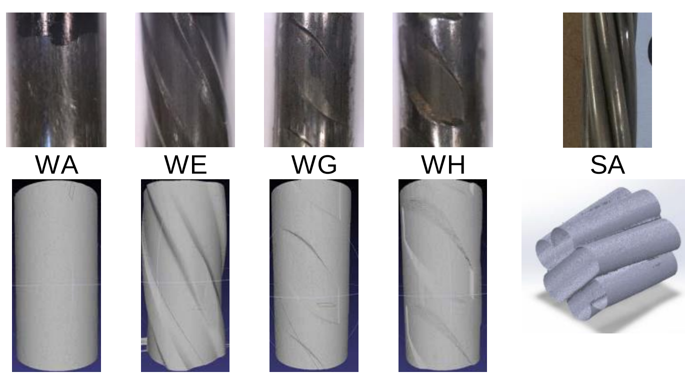

Figure 1. Microscopic images and 3D models (Haynes, 2013) of wires WA, WE, WG, WH and strand SA studied by KSU researchers.

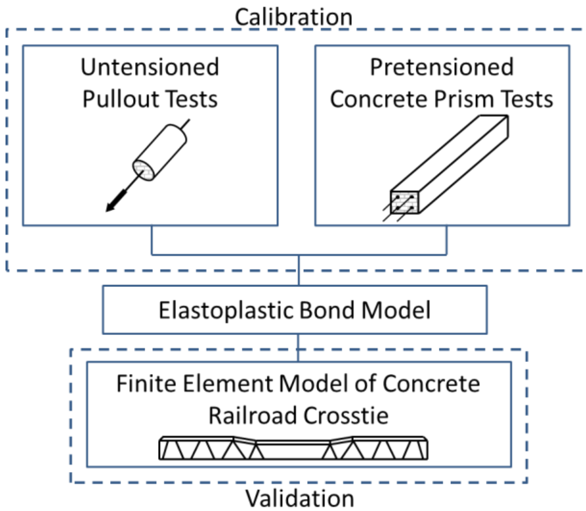

Figure 2. FEA bond modeling framework employed in this study.

2. Elastoplastic bond modeling approach

The commercial FE analysis software Abaqus was employed in this study (Dassault Systèmes, 2012). The concrete material was modeled with concrete damaged plasticity, and the modeling framework and material parameter calibration were described in previous publications (Yu, 2011 and 2012). The elasto-plastic bond model development in this paper follows the general plasticity theory and FE procedure described by Zienkiewicz and Taylor (1991). User subroutines were written for both axisymmetric and 3D cohesive elements in Abaqus, but only the 3D governing equations, similar to the theoretical basis for frictional contact developed by Michalowski and Mroz (1978), are presented here.

2.1 Governing equations

Figure 3 shows the local coordinate system defined for a 3D cohesive element (Dassault Systèmes, 2012). It includes a normal (or thickness) direction and two shear directions, depicted by unit vectors **n**, **s** and **t**, respectively. The traction-displacement constitutive relation type is adopted. The interface stress tensor $\boldsymbol{\sigma}$ includes a normal component σ and two shear components τ_1 and τ_2,

$$\boldsymbol{\sigma} = \sigma\mathbf{n} + \tau_1\mathbf{s} + \tau_2\mathbf{t} \tag{1}$$

The magnitude of the total shear stress is

$$|\tau| = \sqrt{\tau_1^2 + \tau_2^2} \tag{2}$$

The interface displacement tensor $\mathbf{u}$ includes dilation u_n and slips u_{t1} and u_{t2}

$$\mathbf{u} = u_n\mathbf{n} + u_{t1}\mathbf{s} + u_{t2}\mathbf{t} \tag{3}$$

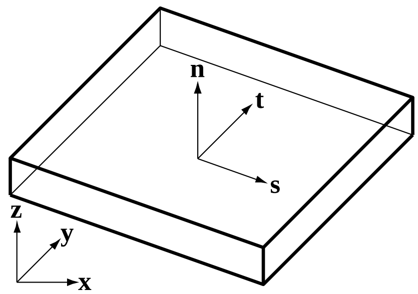

Figure 3. Local coordinate system (n, s, t) for a 3D cohesive element (Dassault Systèmes, 2012).

which can be decomposed into elastic and plastic components

$$\mathbf{u} = \mathbf{u}^{\mathrm{el}} + \mathbf{u}^{\mathrm{pl}} \tag{4}$$

The magnitude of the total plastic slip is written as

$$\left|u_{\mathrm{t}}^{\mathrm{pl}}\right| = \sqrt{\left(u_{\mathrm{t1}}^{\mathrm{pl}}\right)^2 + \left(u_{\mathrm{t2}}^{\mathrm{pl}}\right)^2} \tag{5}$$

Elasticity of the interface material indicates

$$\boldsymbol{\sigma} = \mathbf{D}^{\mathrm{e}}\mathbf{u}^{\mathrm{el}} = \mathbf{D}^{\mathrm{e}}\left(\mathbf{u} - \mathbf{u}^{\mathrm{pl}}\right) \tag{6}$$

where $\mathbf{D}^{\mathrm{e}}$ is the elastic matrix with the dimension force/length[3]. Assuming uncoupled elastic normal-shear behavior, we can write $\mathbf{D}^{\mathrm{e}}$ in the following matrix form

$$\mathbf{D}^{\mathrm{e}} = \begin{bmatrix} D_{\mathrm{nn}}^{\mathrm{e}} & 0 & 0 \\ 0 & D_{\mathrm{ns}}^{\mathrm{e}} & 0 \\ 0 & 0 & D_{\mathrm{nt}}^{\mathrm{e}} \end{bmatrix} \tag{7}$$

where the normal ($D_{\mathrm{nn}}^{\mathrm{e}}$) and shear elastic stiffness ($D_{\mathrm{ns}}^{\mathrm{e}}$, $D_{\mathrm{nt}}^{\mathrm{e}}$) are the only non-trivial components. Isotropy in the shear plane further implies $D_{\mathrm{ns}}^{\mathrm{e}} = D_{\mathrm{nt}}^{\mathrm{e}}$.

For elastic loading and unloading, the yield function F satisfies

$$F < 0 \tag{8}$$

When plastic loading occurs, the stress tensor stays on the yield surface

$$F = 0 \tag{9}$$

The plastic flow rate can be calculated from the plastic potential Q as follows

$$\mathrm{d}\mathbf{u}^{\mathrm{pl}} = \mathrm{d}\lambda \frac{\partial Q}{\partial \boldsymbol{\sigma}} \tag{10}$$

where $\mathrm{d}\mathbf{u}^{\mathrm{pl}}$ is the rate of the plastic interface displacement, and $\mathrm{d}\lambda$ is a proportionality constant. Equation 10 implies an associated flow rule when Q=F and a non-associated flow rule when $Q \neq F$.

2.2 Local iteration

At the element level, updated stress $\boldsymbol{\sigma}$ is sought with given initial stress $\boldsymbol{\sigma}_0$, initial displacement $\mathbf{u}_0$ and incremental displacement $\mathrm{d}\mathbf{u}$. This can be achieved by solving the following equation involving the residual function $\mathbf{R}$,

$$\mathbf{R} = \mathbf{0} \tag{11}$$

The residual function often includes terms of the plastic displacement rate $\mathrm{d}\mathbf{u}^{\mathrm{pl}}$, which can be calculated from the rate form of Equation 6 for elasticity

$$\mathrm{d}\mathbf{u}^{\mathrm{pl}} = \mathrm{d}\mathbf{u} - \mathbf{C}^{\mathrm{e}}\mathrm{d}\boldsymbol{\sigma} \tag{12}$$

where $\mathbf{C}^{\mathrm{e}}$ is the elastic compliance matrix

$$\mathbf{C}^{\mathrm{e}} = \mathbf{D}^{\mathrm{e}-1} \tag{13}$$

Equation 11 is solved by applying the Newton-Raphson method and performing the following substitutive iterations at the element material level until convergence is achieved,

$$\boldsymbol{\sigma}_{i+1} = \boldsymbol{\sigma}_i - \left(\frac{\partial \mathbf{R}}{\partial \boldsymbol{\sigma}}\right)_i^{-1} \mathbf{R}_i \tag{14}$$

where the subscripts "i" and "i+1" indicate the iteration sequence numbers. Convergence is considered to be achieved when the norm of the vector $\mathbf{R}$ is sufficiently small.

2.3 Bond model definitions

Tables 1 shows the yield function, plastic potential, plastic flow rule, residual function and bond material constant definitions for the three types of reinforcements under study: smooth wire, indented wire and seven-wire strand. Table 2 further defines the bond material constant nomenclature.

The adhesive strength a is assumed to depend linearly on the total plastic slip $\left|u_{\mathrm{t}}^{\mathrm{pl}}\right|$,

$$a = \begin{cases} a_0\left(1 - \dfrac{\left|u_{\mathrm{t}}^{\mathrm{pl}}\right|}{u_{\mathrm{tc}}^{\mathrm{pl}}}\right), & \text{if } \left|u_{\mathrm{t}}^{\mathrm{pl}}\right| \le u_{\mathrm{tc}}^{\mathrm{pl}} \\ 0, & \text{if } \left|u_{\mathrm{t}}^{\mathrm{pl}}\right| > u_{\mathrm{tc}}^{\mathrm{pl}} \end{cases} \tag{15}$$

where a_0 is the initial adhesive strength and $u_{\mathrm{tc}}^{\mathrm{pl}}$ the plastic slip at which adhesion (or cohesion) is first broken completely. Equation 15 was applied to all reinforcement types.

Table 1. Yield function, plastic potential, plastic flow rule, residual function and bond material constant definitions.

Definition	Smooth wire	Indented wire	Seven-wire strand
Yield function	$F = \lvert\tau\rvert + \sigma\tan\phi - a$	$F = \sigma + H\left(\tau_1^2 + \tau_2^2 - a^2\right)$	$F = \lvert\tau\rvert + \sigma\tan\phi - a$
Plastic potential	$Q = \lvert\tau\rvert$	$Q = \lvert\tau\rvert + \sigma\tan\psi$	$Q = \lvert\tau\rvert + \sigma\tan\psi$
Plastic flow rule ($\mu_{\mathrm{d}} = \tan\psi$)	$\mathrm{d}u_{\mathrm{n}}^{\mathrm{pl}} = 0$ $\tau_2 \mathrm{d}u_{\mathrm{t1}}^{\mathrm{pl}} = \tau_1 \mathrm{d}u_{\mathrm{t2}}^{\mathrm{pl}}$	$\mathrm{d}u_{\mathrm{n}}^{\mathrm{pl}} = \mu_{\mathrm{d}}\lvert\mathrm{d}u_{\mathrm{t}}^{\mathrm{pl}}\rvert$ $\tau_2 \mathrm{d}u_{\mathrm{t1}}^{\mathrm{pl}} = \tau_1 \mathrm{d}u_{\mathrm{t2}}^{\mathrm{pl}}$	$\lvert\tau\rvert\tan\psi \mathrm{d}u_{\mathrm{t1}}^{\mathrm{pl}} = \tau_1 \mathrm{d}u_{\mathrm{n}}^{\mathrm{pl}}$ $\lvert\tau\rvert\tan\psi \mathrm{d}u_{\mathrm{t2}}^{\mathrm{pl}} = \tau_2 \mathrm{d}u_{\mathrm{n}}^{\mathrm{pl}}$
Residual function in local iteration	$\mathbf{R} = \begin{Bmatrix} F \\ \mathrm{d}u_{\mathrm{n}}^{\mathrm{pl}} \\ \tau_2 \mathrm{d}u_{\mathrm{t1}}^{\mathrm{pl}} - \tau_1 \mathrm{d}u_{\mathrm{t2}}^{\mathrm{pl}} \end{Bmatrix}$	$\mathbf{R} = \begin{Bmatrix} F \\ \mu_{\mathrm{d}}\lvert\mathrm{d}u_{\mathrm{t}}^{\mathrm{pl}}\rvert - \mathrm{d}u_{\mathrm{n}}^{\mathrm{pl}} \\ \tau_2 \mathrm{d}u_{\mathrm{t1}}^{\mathrm{pl}} - \tau_1 \mathrm{d}u_{\mathrm{t2}}^{\mathrm{pl}} \end{Bmatrix}$	$\mathbf{R} = \begin{Bmatrix} F \\ \lvert\tau\rvert\tan\psi \mathrm{d}u_{\mathrm{t1}}^{\mathrm{pl}} - \tau_1 \mathrm{d}u_{\mathrm{n}}^{\mathrm{pl}} \\ \lvert\tau\rvert\tan\psi \mathrm{d}u_{\mathrm{t2}}^{\mathrm{pl}} - \tau_2 \mathrm{d}u_{\mathrm{n}}^{\mathrm{pl}} \end{Bmatrix}$
Bond material constant	$D_{\mathrm{nn}}^{\mathrm{e}}$, $D_{\mathrm{ns}}^{\mathrm{e}} (= D_{\mathrm{nt}}^{\mathrm{e}})$, $\tan\phi$, a_0, $u_{\mathrm{tc}}^{\mathrm{pl}}$	$D_{\mathrm{nn}}^{\mathrm{e}}$, $D_{\mathrm{ns}}^{\mathrm{e}} (= D_{\mathrm{nt}}^{\mathrm{e}})$, a_0, $u_{\mathrm{tc}}^{\mathrm{pl}}$, $u_{\mathrm{td}}^{\mathrm{pl}}$, $u_{\mathrm{ts}}^{\mathrm{pl}}$, H_0, H_1, $\mu_{\mathrm{d}}^{\max}$	$D_{\mathrm{nn}}^{\mathrm{e}}$, $D_{\mathrm{ns}}^{\mathrm{e}} (= D_{\mathrm{nt}}^{\mathrm{e}})$, $\tan\phi$, a_0, $u_{\mathrm{tc}}^{\mathrm{pl}}$, $\tan\psi$

Table 2. Bond material constant nomenclature.

Constant	Description	Constant	Description
$D_{\mathrm{nn}}^{\mathrm{e}}$	Normal elastic stiffness	$D_{\mathrm{ns}}^{\mathrm{e}} (= D_{\mathrm{nt}}^{\mathrm{e}})$	Shear elastic stiffness
$\tan\phi$	Coefficient of friction	$\tan\psi$	Dilatational coefficient
a_0	Initial adhesive strength	$u_{\mathrm{tc}}^{\mathrm{pl}}$	Plastic slip at which adhesion (or cohesion) breaks completely
$u_{\mathrm{td}}^{\mathrm{pl}}$	Plastic slip at which dilatational coefficient starts to decrease	$u_{\mathrm{ts}}^{\mathrm{pl}}$	Plastic slip at which interface sliding initiates
H_0	Initial hardening parameter	H_1	Ultimate hardening parameter
$\mu_{\mathrm{d}}^{\max}$	Maximum dilatational coefficient		

For the three indented wires, the following form is assumed for the hardening parameter H:

$$H = \begin{cases} H_0, & \text{if } \lvert u_{\mathrm{t}}^{\mathrm{pl}}\rvert \le u_{\mathrm{tc}}^{\mathrm{pl}} \\ H_0 + \dfrac{H_1 - H_0}{u_{\mathrm{ts}}^{\mathrm{pl}} - u_{\mathrm{tc}}^{\mathrm{pl}}}\left(\lvert u_{\mathrm{t}}^{\mathrm{pl}}\rvert - u_{\mathrm{tc}}^{\mathrm{pl}}\right), & \text{if } u_{\mathrm{tc}}^{\mathrm{pl}} < \lvert u_{\mathrm{t}}^{\mathrm{pl}}\rvert \le u_{\mathrm{ts}}^{\mathrm{pl}} \\ H_1, & \text{if } \lvert u_{\mathrm{t}}^{\mathrm{pl}}\rvert > u_{\mathrm{ts}}^{\mathrm{pl}} \end{cases} \tag{16}$$

where H_0 and H_1 are initial and ultimate hardening parameters, respectively, and $u_{\mathrm{ts}}^{\mathrm{pl}}$ is the plastic slip at which an ultimate sliding stage is reached.

It is noted that the plastic dilatation rates for the interfaces of the indented wires and seven-wire strand are nonzero and instead scaled with the plastic slip rates by a factor of $\tan\psi$ (see definitions of plastic flow rule in Table 1). The dilatational coefficient $\tan\psi$ is assumed to be constant for the seven-wire strand. The dilatational coefficient is denoted as μ_{d} for the indented wires and assumed to be a function of the total plastic slip in the following form

$$\mu_{\mathrm{d}} = \begin{cases} \mu_{\mathrm{d}}^{\max}, & \text{if } \left|u_{\mathrm{t}}^{\mathrm{pl}}\right| \le u_{\mathrm{td}}^{\mathrm{pl}} \\ \dfrac{\mu_{\mathrm{d}}^{\max}}{u_{\mathrm{td}}^{\mathrm{pl}} - u_{\mathrm{ts}}^{\mathrm{pl}}}\left(\left|u_{\mathrm{t}}^{\mathrm{pl}}\right| - u_{\mathrm{ts}}^{\mathrm{pl}}\right), & \text{if } u_{\mathrm{td}}^{\mathrm{pl}} < \left|u_{\mathrm{t}}^{\mathrm{pl}}\right| \le u_{\mathrm{ts}}^{\mathrm{pl}} \\ 0, & \text{if } \left|u_{\mathrm{t}}^{\mathrm{pl}}\right| > u_{\mathrm{ts}}^{\mathrm{pl}} \end{cases} \tag{17}$$

where $\mu_{\mathrm{d}}^{\max}$ is the maximum dilatational coefficient and $u_{\mathrm{td}}^{\mathrm{pl}}$ the plastic slip at which μ_{d} starts to decrease linearly from $\mu_{\mathrm{d}}^{\max}$. The dilatational coefficient μ_{d} is assumed to reach 0 at $u_{\mathrm{ts}}^{\mathrm{pl}}$.

2.4 Global stiffness matrix

In incremental FE analyses, the user material's Jacobian matrix $\mathbf{D}^{\mathrm{ep}}$ is sought to determine the stress increment $\mathrm{d}\boldsymbol{\sigma}$ in terms of the displacement increment $\mathrm{d}\mathbf{u}$,

$$\mathrm{d}\boldsymbol{\sigma} = \mathbf{D}^{\mathrm{ep}}\mathrm{d}\mathbf{u} \tag{18}$$

This element stiffness matrix is passed on to assemble the stiffness matrix used in the global iterations and therefore also referred to as the global stiffness matrix of the element.

Based on definitions in Table 1, $\mathbf{D}^{\mathrm{ep}}$ can be obtained for the smooth wire and the seven-wire strand as follows

$$\mathbf{D}^{\mathrm{ep}} = \mathbf{D}^{\mathrm{e}} - \frac{\mathbf{D}^{\mathrm{e}}\dfrac{\partial Q}{\partial \boldsymbol{\sigma}}\left(\dfrac{\partial F}{\partial \boldsymbol{\sigma}}\right)^{\mathrm{T}}\mathbf{D}^{\mathrm{e}}}{\left(\dfrac{\partial F}{\partial \boldsymbol{\sigma}}\right)^{\mathrm{T}}\mathbf{D}^{\mathrm{e}}\dfrac{\partial Q}{\partial \boldsymbol{\sigma}} - \dfrac{\partial F}{\partial a}\left(\dfrac{\partial a}{\partial \mathbf{u}^{\mathrm{pl}}}\right)^{\mathrm{T}}\dfrac{\partial Q}{\partial \boldsymbol{\sigma}}} \tag{19}$$

whereas $\mathbf{D}^{\mathrm{ep}}$ for the indented wires is

$$\mathbf{D}^{\mathrm{ep}} = \mathbf{D}^{\mathrm{e}} - \frac{\mathbf{D}^{\mathrm{e}}\dfrac{\partial Q}{\partial \boldsymbol{\sigma}}\left(\dfrac{\partial F}{\partial \boldsymbol{\sigma}}\right)^{\mathrm{T}}\mathbf{D}^{\mathrm{e}}}{\left(\dfrac{\partial F}{\partial \boldsymbol{\sigma}}\right)^{\mathrm{T}}\mathbf{D}^{\mathrm{e}}\dfrac{\partial Q}{\partial \boldsymbol{\sigma}} - \left[\dfrac{\partial F}{\partial H}\left(\dfrac{\partial H}{\partial \mathbf{u}^{\mathrm{pl}}}\right)^{\mathrm{T}} + \dfrac{\partial F}{\partial a}\left(\dfrac{\partial a}{\partial \mathbf{u}^{\mathrm{pl}}}\right)^{\mathrm{T}}\right]\dfrac{\partial Q}{\partial \boldsymbol{\sigma}}} \tag{20}$$

3. Calibration of bond material constants

The KSU untensioned pullout and pretensioned prism test data (Arnold, 2013; Bodapati, 2013a) were employed to calibrate the bond material constants listed in Table 1.

An untensioned pullout test has a wire (with a nominal diameter of 0.209 in. or 5.32 mm) or a strand (with a nominal diameter of 3/8 in. or 9.525 mm) embedded in a concrete matrix and pulled at one end. The pullout force and the displacements at the unloaded and loaded ends of the steel reinforcement were recorded. The bond stress can be calculated based on the pullout force and the specimen geometry. Axisymmetric models were developed to simulate this test.

The concrete prisms used in the pretensioned prism tests were 69 in. (1.75 m) long. There were four wires or four strands, in 2 by 2 arrangements, embedded in the concrete matrix. The prisms embedded with the wires measured 3.5 in. (88.9 mm) on each side of the cross section, and every two wires were spaced 1.5 in. (38.1 mm) apart. The prisms embedded with the strands measured 5.5 in. (139.7 mm) on each side of the cross section, and every two strands were spaced 2 in. (50.8 mm) apart. The wires in the concrete prisms were pretensioned to 7,000 pound force (31,137 N), equivalent to a nominal initial tensile stress of 203 ksi (1,399.6 MPa). The strands in the concrete prisms were pretensioned to 17,415 pound force (77,466 N), equivalent to a nominal initial tensile stress of 158 ksi (1,089.4 MPa). Once the concrete reached a desired compressive strength, the pretension was released with the wires/strands cut at the prism ends. The concrete prisms were tested with three release strengths: 3,500, 4,500 and 6,000 psi (24.1, 31.0 and 41.4 MPa), while simulations used test data corresponding to a concrete release strength of 6,000 psi (41.4 MPa). Concrete surface strains were then measured for each prism and used to calculate the transfer length. In modeling, quarter symmetry in the cross section and half symmetry over the length were assumed, resulting in one-eighth of the prism being modeled.

It is noted that due to logistic reasons, the concrete strain could not be measured at the same time the wire/strand pretension was released, and the time lapse between the two events led to considerable concrete creep by the time the strain measurements were taken. As a result, the measured concrete surface strains were consistently higher than FE predictions. To be able to make meaningful comparisons between the test data and the simulation results, a method was developed to account for the added strain due to creep.

Bazant and Baweja (2000) postulated that for a constant uniaxial stress σ within the service range and applied at age t', the strain ε at age t can be written as

$$\varepsilon(t) = J(t,t')\sigma + \varepsilon_{\mathrm{sh}}(t) + \alpha \Delta T(t) \tag{21}$$

where J is the compliance function, $\varepsilon_{\mathrm{sh}}$ the shrinkage strain, α the thermal expansion coefficient, and ΔT the temperature change. The compliance function can be further expressed in elastic and creep terms as

$$J(t,t') = 1/E(t') + C_0(t,t') + C_{\mathrm{d}}(t,t',t_0) \tag{22}$$

where $E(t')$ is the modulus of elasticity at loading age t', $C_0(t,t')$ is the basic creep compliance, and $C_{\mathrm{d}}(t,t',t_0)$ is the creep compliance due to simultaneous drying. Considering only the basic creep mechanism, we rewrite Equation 21 as

$$\varepsilon(t) = \sigma/E(t') + \sigma C_0(t,t') \tag{23}$$

Further assuming that at age t'

$$\sigma = E(t')\varepsilon(t') \tag{24}$$

we have an estimate of $C_0(t,t')$ as follows,

$$C_0(t,t') = \frac{\varepsilon(t) - \varepsilon(t')}{E(t')\varepsilon(t')} \tag{25}$$

C_0 can be estimated from Equation 25 by substituting $\varepsilon(t)$ for the average maximum test measurement and $\varepsilon(t')$ for the average maximum FE prediction for the concrete surface strain,

$$C_0 \approx \frac{AMS(\varepsilon_{\text{test}}) - AMS(\varepsilon_{\text{FE}})}{E_c AMS(\varepsilon_{\text{FE}})} \tag{26}$$

where *AMS* stands for the average maximum strain, and E_c is Young's modulus of concrete. The FE predicted strain along the length of the prism can then be adjusted with the creep strain according to Equation 23 and compared with the measured strain data,

$$\begin{aligned} \varepsilon_{\text{FE-adjusted}} &= \sigma / E_c + \sigma C_0 \\ &= \varepsilon_{\text{FE}} + \sigma C_0 \end{aligned} \tag{27}$$

Bond material constants (see definitions in Table 1 and Table 2) were initially assigned and iteratively adjusted until simulation results compared favorably with the corresponding test data for both untensioned pullout tests and pretensioned prism tests. Table 3 shows the concrete and steel material parameters used in the simulations of the tests. For untensioned pullout tests, the predicted bond stress vs. unloaded end slip curves were compared with the corresponding test data. For pretensioned prism tests, the predicted concrete surface strain profile adjusted with creep strain was compared with the corresponding test data. This calibration process yielded the bond material constants shown in Table 4 for all four wires and the sever-wire strand. Detailed calibration procedures and results are described in previous publications (Yu and Jeong, 2014, 2015 and 2016).

Table 3. Concrete and steel material parameters used in the simulations of untensioned pullout and pretensioned prism tests.

Concrete		Steel (wire)		Steel (strand)	
Young's modulus	4,028 ksi (27.8 GPa)	Young's modulus	30,000 ksi (206.8 GPa)	Young's modulus	30,000 ksi (206.8 GPa)
Tensile strength	478.8 psi (3.3 MPa)	Yield strength	274,000 psi (1,889.2 MPa)	Yield strength	270,600 psi (1,865.7 MPa)
Compressive strength	5977.8 psi (41.2 MPa)				

Table 4. Calibrated bond material constants.

Symbol	Smooth wire WA	Seven-wire strand SA
D^{e}_{nn}	12,889,494 lbf/in^3 (3,498.8 N/mm^3)	92,630,000 lbf/in^3 (25,144.1 N/mm^3)
$D^{e}_{ns}(= D^{e}_{nt})$	268,531 lbf/in^3 (72.9 N/mm^3)	385,958 lbf/in^3 (104.8 N/mm^3)
$\tan\phi$	0.45	0.3
$\tan\psi$	-	0.0036
a_0	253 psi (MPa)	600 psi (4.14 MPa)
u^{pl}_{tc}	0.077 in. (mm)	0.08 in. (2.03 mm)

Symbol	Indented wire WE	Indented wire WG	Indented wire WH
D^{e}_{nn}	12,889,494 lbf/in^3 (3,498.8 N/mm^3)	12,889,494 lbf/in^3 (3,498.8 N/mm^3)	12,889,494 lbf/in^3 (3,498.8 N/mm^3)
$D^{e}_{ns}(=D^{e}_{nt})$	268,531 lbf/in^3 (72.9 N/mm^3)	268,531 lbf/in^3 (72.9 N/mm^3)	268,531 lbf/in^3 (72.9 N/mm^3)
a_0	550 psi (3.79 MPa)	400 psi (2.76 MPa)	1000 psi (6.89 MPa)
u^{pl}_{tc}	0.04 in. (1.02 mm)	0.04 in. (1.02 mm)	0.04 in. (1.02 mm)
u^{pl}_{td}	0.14 in. (3.56 mm)	0.17 in. (4.32 mm)	0.26 in. (6.60 mm)
u^{pl}_{ts}	0.15 in. (3.81 mm)	0.18 in. (4.57 mm)	0.27 in. (6.86 mm)
H_0	0.0012 psi^{-1} (0.174 MPa^{-1})	0.0022 psi^{-1} (0.319 MPa^{-1})	0.001 psi^{-1} (0.145 MPa^{-1})
H_1	0.0012 psi^{-1} (0.174 MPa^{-1})	0.005 psi^{-1} (0.725 MPa^{-1})	0.018 psi^{-1} (2.611 MPa^{-1})
μ^{max}_{d}	0.01	0.014	0.013

4. Validation with test data

Concrete crossties were made at a plant with 20 prestressing wires or 8 seven-wire strands. Figure 4 shows full end and side views of the FE mesh of the tie models. Compared to the pretensioned prisms tested in the lab, the ties are non-prismatic, and there are eight scallops on each side of the ties. The same pretensioning forces employed in the laboratory phase were applied in the plant phase. Quarter symmetric tie models were developed, and pretension release in these ties was simulated. The concrete and steel material parameters in Table 3 were applied in all concrete tie models. The calibrated bond material constants in Table 4 for each specific reinforcement type were applied in the respective concrete tie models made of these reinforcements.

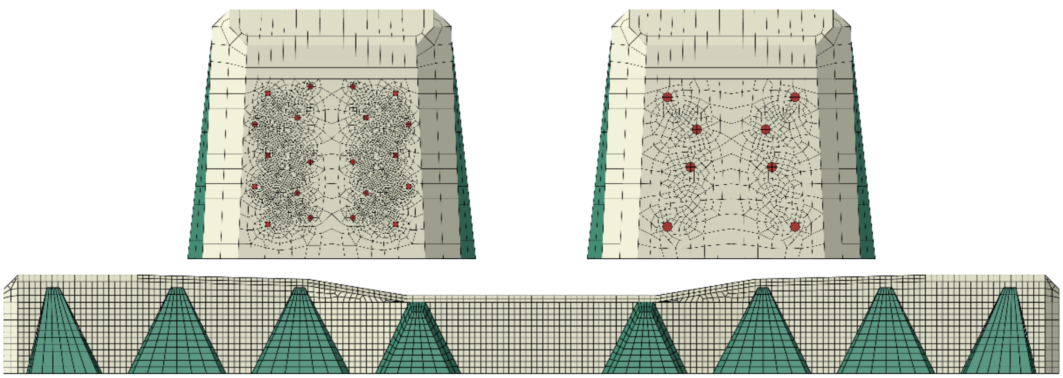

Figure 4. Full end views of the FE mesh for the 20-wire (top left) and 8-strand concrete crosstie models (top right) and the full side view (bottom).

In the plant, the concrete strain profiles along the bottom surface of the ties were measured after the pretension release process was completed (Bodapati, 2013b). Two strain measuring methods were employed: Whittemore gauge and Laser Speckle Imaging (LSI). Again the measured concrete surface strain had significant creep components, and the FE predicted surface strain was adjusted with creep strain according to Equations 26 and 27. The adjusted FE prediction was then compared with the test data for validation of our FE models.

4.1 Smooth wire

Figure 5 compares the concrete surface strain profiles measured using the LSI technique with those obtained in the simulation of the crosstie made with 20 smooth wires. The gray lines are measurements made on individual ties. The average test curve is also plotted. The simulation curve without creep adjustment generally shows lower strain than the test curves. Following a creep strain adjustment with a creep compliance of C_0=0.138 microstrain/psi (20.02 microstrain/MPa), the simulation curve agrees well with the average test curve not only in magnitudes but also in the general curve shape.

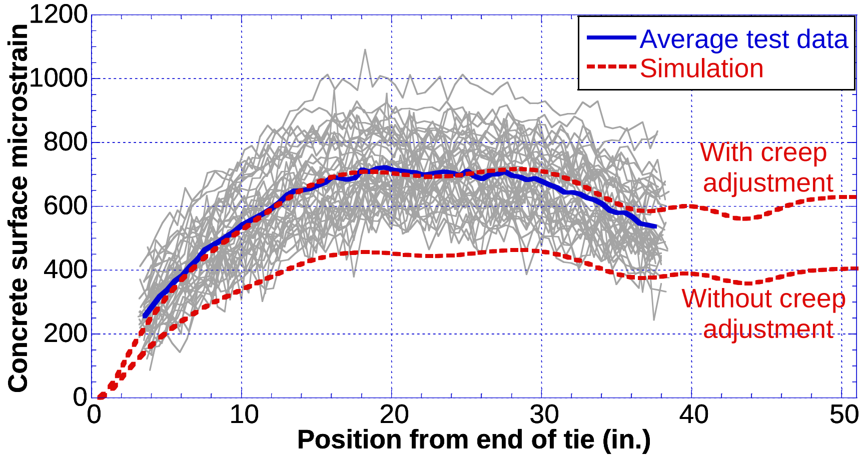

Figure 5. Measured vs. model predicted surface strain profiles in concrete crossties made with 20 smooth wires (1 in. = 25.4 mm).

4.2 Indented wires

For concrete ties made with the indented wires WE, WG or WH, strain data measured from Whittemore gauges were compared with the FE simulation results. Figure 6 compares the averages of six Whittemore gauge measurements with the creep adjusted FE strain for concrete ties made with each wire. The estimated creep compliance parameters C_0 were 0.173, 0.199 and 0.201 microstrain/psi (25.09, 28.86 and 29.15 microstrain/MPa), respectively, for wires WE, WG and WH. The simulation results agree reasonably well with the test data.

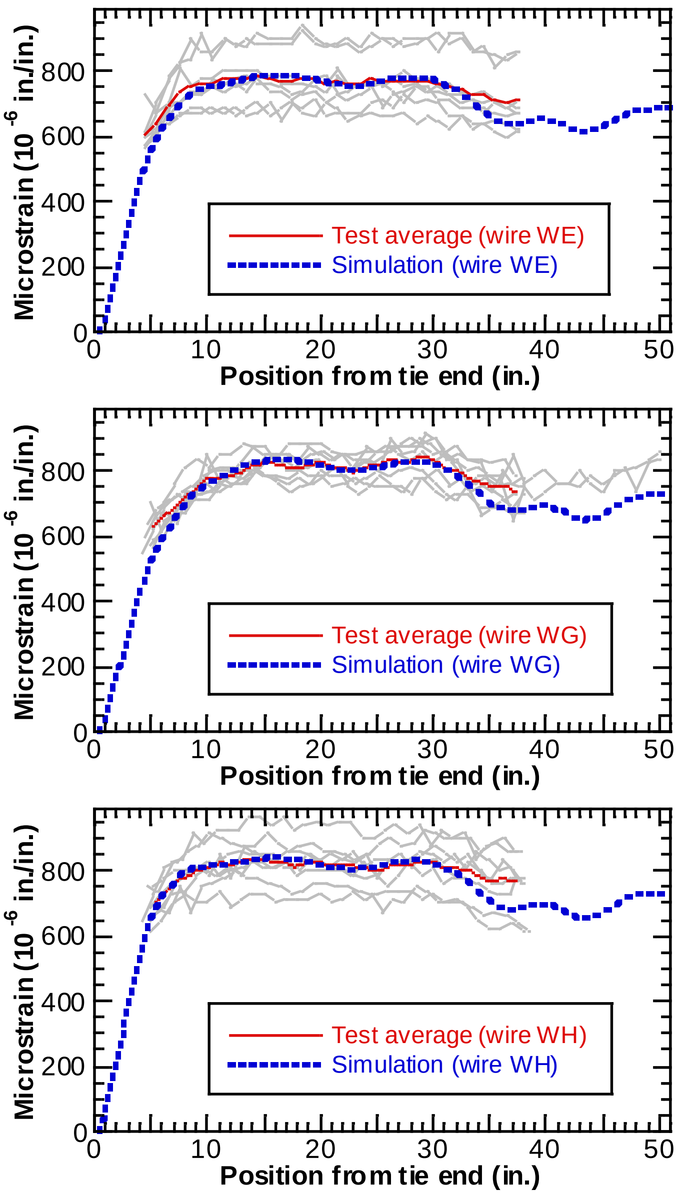

Figure 6. Measured versus FE predicted (with creep strain adjustment) surface strain profiles of plant made concrete crossties, each with 20 indented wires (1 in. = 25.4 mm).

4.3 Seven-wire strand

For concrete ties made with the seven-wire strand, again FE simulations of the pretension release process were conducted. To compare with the FE results, strain data from both Whittemore gauge and LSI were examined, yielding C_0's of 0.17 and 0.096 microstrain/psi (24.7 and 13.9 microstrain/MPa), respectively. To enable direct comparisons of all three sets of data (FE, Whittemore gauge and LSI), the creep strain was removed from the test data by an inverse operation to Equation 27,

$$\varepsilon_{\text{test-adjusted}} = \frac{\varepsilon_{\text{test}}}{1 + E_c C_0} \tag{28}$$

The adjusted test data are then plotted along with the FE predicted strain in Figure 7. The test curves were calculated according to Equation 28 based on averages of multiple measurement data. The FE results appear to fall within the scattering of the experimental data obtained from the two strain measuring methods.

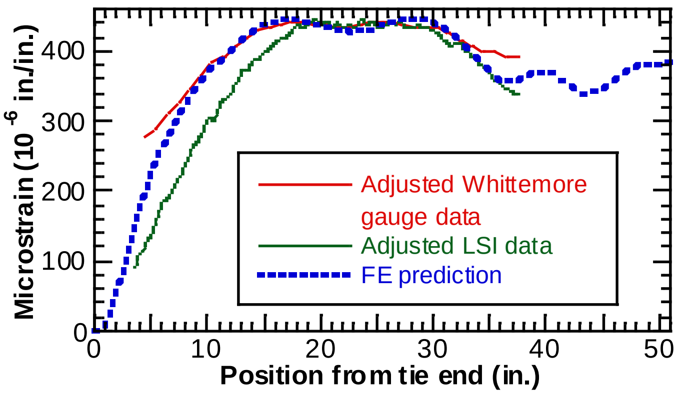

Figure 7. Adjusted Whittemore gauge and LSI measurements versus FE prediction of the surface strain profile of plant made concrete crossties with 8 seven-wire strands (1 in. = 25.4 mm).

5. Summary and conclusions

Elasto-plastic bond models were developed for the interfaces between concrete and five prestressing wires or strand, including a smooth wire, three indented wires and a seven-wire strand. The theoretical development and numerical implementation of the bond models with the cohesive elements in Abaqus are described in this paper. A significant feature of the bond models in this paper is the ability to reproduce the dilatational effect in the interface as bond-slip occurs, so the splitting propensity of the adjacent concrete can be accounted for realistically. The bond material constants were calibrated from laboratory wire/strand pullout and pretensioned prism tests conducted on concrete specimens embedded with the respective reinforcements. The bond models were further validated with concrete surface strain profiles measured on actual concrete ties made at a plant. The comprehensive set of bond models is now available for studies of railroad concrete crosstie behavior using the FE analysis method.

6. Acknowledgement

The work described in this paper was sponsored by the Office of Research, Development and Technology, Federal Railroad Administration, U.S. Department of Transportation. Directions provided by Messrs. Gary Carr and Cameron Stuart of the Track Research Division are gratefully acknowledged. The authors would also like to thank Professors Robert J. Peterman, B. Terry Beck and John Wu of Kansas State University for sharing the test data applied in this study.

7. References

1. Arnold, M. L., Peterman, R. J., Bodapati, N. N. B., Beck, B. T., and Wu, C. H. J., 2013, "Development of a Standard Bond Test for Indented Prestressing Wires," Proc. 2013 Joint Rail Conference, JRC2013-2461.
2. Bazant, Z. P., and Baweja, S., 2000, "Creep and Shrinkage Prediction Model for Analysis and Design of Concrete Structures: Model B3," ACI Special Publications, 194, pp. 1-84.
3. Bodapati, N. N. B., Zhao, W., Peterman, R. J., Wu, C. H. J., Beck, B. T., Haynes, M., and Holste, J. R., 2013a, "Influence of Indented Wire Geometry and Concrete Parameters on the Transfer Length in Pretensioned Concrete Crossties," Proc. 2013 Joint Rail Conference, JRC2013-2463.
4. Bodapati, N. N. B., Peterman, R. J., Zhao, W., Beck, B. T., Wu, C. H. J., Holste, J. R., Arnold, M. L., Benteman, R., and Schweiger, R., 2013b, "Transfer-Length Measurements on Concrete Railroad Ties Fabricated with 15 Different Prestressing Reinforcements," Proc. 2013 PCI Convention and National Bridge Conference.
5. Dassault Systèmes, 2012, Abaqus Analysis User's Manual.
6. Haynes, M., Wu, C. H. J., Beck, B. T., Bodapati, N. N. B., and Peterman, R. J., 2013, "Prestressing Steel Reinforcement Wire Bond Index Number," Proc. 2013 Joint Rail Conference, JRC2013-2422, American Society of Mechanical Engineers.
7. Michalowski, R., and Mroz, Z., 1978, "Associated and Non-Associated Sliding Rules in Contact Friction Problems," Archives of Mech., 30(3), pp. 259-276.
8. Yu, H., Jeong, D. Y., Choros, J., and Sussmann, T., 2011, "Finite Element Modeling of Prestressed Concrete Crossties with Ballast and Subgrade Support." Proc. ASME 2011 International Design Engineering Technical Conferences & Computers and Information in Engineering Conference, DETC2011-47452.
9. Yu, H., and Jeong, D. Y., 2012, "Railroad Tie Responses to Directly Applied Rail Seat Loading in Ballasted Tracks: A Computational Study," Proc. ASME/ASCE/IEEE 2012 Joint Rail Conference, JRC2012-74149.
10. Yu, H., and Jeong, D. Y., 2014, "Bond between Smooth Prestressing Wires and Concrete: Finite Element Model and Transfer Length Analysis for Pretensioned Concrete Crossties," Proceedings of the 2014 ASCE Structures Congress.

11. Yu, H., and Jeong, D.Y., 2015, "Finite Element Bond Models for Seven-Wire Prestressing Strands in Concrete Crossties," Proceedings of the 2015 Joint Rail Conference, JRC2015-5758.
12. Yu, H., and Jeong, D.Y., 2016, "Finite Element Bond Modeling for Indented Wires in Pretensioned Concrete Crossties," 2016 Joint Rail Conference, JRC2016-5782.
13. Zhao, W., Beck, B. T., Peterman, R. J., Wu, C. H. J., Bodapati, N. N. B., and Lee, G., 2014, "Reliable Transfer Length Assessment for Real-Time Monitoring of Railroad Crosstie Production," Proc. 2014 Joint Rail Conference, JRC2014-3830, American Society of Mechanical Engineers.
14. Zienkiewicz, O. C., and Taylor, R. L., 1991, The Finite Element Method. Vol. 2. Solid and Fluid Mechanics Dynamics and Non-Linearity, Fourth Edition, McGraw-Hill, London.